Running title: Myosins power endocytosis

An endocytic myosin essential for plasma membrane invagination powers motility against resistance

Ross TA Pedersen[1, 3, 4], Aaron Snoberger[2, 4], Serapion Pyrpassopoulos[2], Daniel Safer[2], David G Drubin[1*], E Michael Ostap[2*]

[1]Department of Molecular and Cell Biology, University of California, Berkeley, Berkeley, CA 94720

[2]Pennsylvania Muscle Institute, Perelman School of Medicine, University of Pennsylvania, Philadelphia, PA 19104

[3]Present address: Department of Embryology, Carnegie Institution for Science, Baltimore, MD 21218

[4]Equal Contribution

*Correspondence: drubin@berkeley.edu, ostap@mail.med.upenn.edu

Abstract

Assembling actin filaments work together with myosins to accomplish a wide array of biological processes. During clathrin-mediated endocytosis (CME), actin assembly and type I myosin cooperate to bend the plasma membrane into a pit that undergoes scission to internalize a cargo-bearing vesicle. How actin assembly and myosin work together in this process is a critical, unanswered question. Some type I myosins directly power motility, while others act as force-sensitive clamps. The *Saccharomyces cerevisiae* endocytic type I myosin Myo5 has been meticulously studied *in vivo*, yet whether this protein's essential CME function is to power membrane invagination or to bind to force-bearing actin filaments to collect and organize them for optimal force production has not been established. We report that Myo5 is a low-duty-ratio motor with a working stroke that is rapid and force-insensitive compared to related myosins that act as force-sensitive anchors. We therefore propose that Myo5 generates power to augment actin assembly-based forces during endocytosis.

Introduction

During clathrin-mediated endocytosis (CME), the plasma membrane invaginates into a pit and undergoes scission to become a cytoplasmic vesicle. The endocytic coat can deform membranes and stabilize curvature for membranes under low tension (Dannhauser and Ungewickell, 2012; Busch et al., 2015; Cail et al., 2022), but in the cell, bending is resisted by membrane tension (Hassinger et al., 2017). Under conditions of high membrane tension, the actin cytoskeleton assists plasma membrane invagination (Boulant et al., 2011; Kaplan et al., 2022). In yeasts, including *Saccharomyces cerevisiae* and *Schizosaccharomyces pombe*, turgor pressure uniformly opposes plasma membrane invagination, so actin assembly is required at every CME site (Aghamohammadzadeh and Ayscough, 2009; Basu et al., 2013). This consistent requirement for actin assembly has made yeasts particularly useful organisms for studying the mechanism by which actin powers membrane deformation during CME.

The actin cytoskeleton can produce pushing and pulling force, both of which are required for CME in *S. cerevisiae* (Sun et al., 2006). When actin filament ends grow against a surface, they push the surface forward, powering motility (Mogilner and Oster, 1996, 2003). During CME, actin filaments bind to coat proteins at the tip of the endocytic invagination (Skruzny et al., 2012), and the filaments grow when new monomers are added at the base of the endocytic site, causing filaments to push against the plasma membrane (Picco et al., 2015; Kaksonen et al., 2005, 2003, Fig. 1). Modeling of the homologous CME actin machinery in mammalian cells has demonstrated that a growing network with this geometry can generate sufficient power for CME (Akamatsu et al., 2020), but whether the

61 power of actin assembly alone can overcome turgor pressure in yeast cells is under debate
62 (Nickaeen et al., 2019; Carlsson, 2018).

63 Myosins, on the other hand, couple ATP hydrolysis to conformational changes that
64 pull on actin filaments. The myosins critical for CME, Myo3 and Myo5 in budding yeast, and
65 Myo1e in mammalian cells, are type I myosins (Geli and Riezman, 1996; Cheng et al., 2012;
66 Krendel et al., 2007). Proper regulation of endocytic myosins is critical for healthy cell
67 function, as overexpression of Myo1e has recently been discovered to be correlated with
68 adverse outcomes in lung adenocarcinoma patients (Jusue-Torres et al., 2023). Within the
69 type I myosin family, some motors are optimized to generate power – i.e., they carry out
70 mechanical work per unit time by consuming ATP to carry out a power stroke. Other type I
71 myosins are more ideally suited to serve as force-sensitive anchors – their ATPase cycle is
72 easily arrested by resistive force, locking them in a state that maintains static tension
73 without completing the ATPase cycle or powering movement (Greenberg and Ostap, 2013).
74 For example, detachment of rat Myo1b from actin filaments slows dramatically under
75 modest resistive forces, making this motor unlikely to power motility but ideally suited to
76 hold tension (Laakso et al., 2008). A closely related enzyme, mouse Myo1c, has actin
77 detachment kinetics that are much less sensitive to resistive forces. It takes ~5 pN of
78 resistive force to slow Myo1c's detachment to the same degree that ~1 pN of resistive force
79 slows Myo1b's detachment, making Myo1c more ideally suited to generate power and
80 transport cellular materials (Greenberg et al., 2012). The possible roles of type I myosins in
81 CME depend on whether endocytic myosins are power generators or force-sensitive
82 anchors.

83 Type I myosins could organize actin filaments within this endocytic actin network or
84 they could displace filaments, invaginating the plasma membrane and facilitating actin
85 growth by creating space for monomers to bind onto barbed ends (Evangelista et al., 2000).
86 Myosin-1 motors are organized in a ring at the base of endocytic sites, where the
87 invaginated membrane meets the plasma membrane (Mund et al., 2018, Fig. 1). Yeast type I
88 myosins serve at least one organizational function as a membrane anchor for the actin
89 assembly machinery, which is associated with the non-motor tail of the molecules
90 (Pedersen and Drubin, 2019; Lewellyn et al., 2015). A mutant Myo5 protein lacking the
91 sequence encoding its motor domain can suffice as a membrane anchor for the actin
92 network, but cannot facilitate endocytic internalization (Pedersen and Drubin, 2019). Thus,
93 if Myo5 is a force sensitive anchor, its essential role in CME may be to hold growing
94 filaments in an optimal orientation for force generation (Fig. 1, left). On the other hand, the
95 rate of actin assembly at CME sites depends on the type I myosin motors in a dose-
96 dependent manner (Manenschijn et al., 2019). If these Myosins are power-generating
97 motors, they may pull actin filament ends away from the plasma membrane, deepening the
98 plasma membrane invagination and creating space for monomer addition and filament
99 elongation (Fig. 1, right).
100 To distinguish between these possibilities, we measured the force sensitivity of the
101 *S. cerevisiae* endocytic type I myosin Myo5 (not to be confused with the vertebrate type-V
102 myosin). We find that Myo5 motor kinetics are insensitive to resistive force compared to
103 related myosins. We therefore propose that Myo5 actively powers CME. Because actin and
104 myosin contribute to a variety of membrane remodeling processes, we expect that these
105 results will be instructive beyond CME.

Results and Discussion

Heavy Chain Phosphorylation Activates Myo5 ATPase Activity

To measure the force sensitivity of Myo5 kinetics, we first established a baseline by measuring Myo5 kinetics in the absence of force. We purified, from *S. cerevisiae*, a Myo5 construct containing the motor and lever arm domains. Because phosphorylation of Myo5 at the TEDS site is required for most CME events and is thought to regulate Myo5's motor activity (Grosshans et al., 2006; Sun et al., 2006; Bement and Mooseker, 1995), we purified a phosphorylated version and an unphosphorylated version of the protein separately (See Materials and methods, Fig 2A). The yeast light chain for Myo5, calmodulin (Cmd1, Geli et al., 1998) was expressed in *E. coli*, purified separately from Myo5, and included in excess in all experiments (See Materials and methods, Fig. 2A).

The steady-state actin-activated ATPase activities of phosphorylated and unphosphorylated Myo5 were determined using the NADH-coupled assay (De La Cruz and Ostap, 2009) in the presence of 0 - 80 μM phalloidin-stabilized actin. Unphosphorylated Myo5 ATPase activity was largely insensitive to actin: the ATPase rate for unphosphorylated Myo5 at 0 μM actin was 0.14 s^{-1}, while the maximum ATPase rate measured was 0.39 s^{-1} at 40 μM actin. (Fig. 2B). Phosphorylation activated Myo5 ATPase activity by about 10-fold. The actin concentration dependence of the phosphorylated Myo5 ATPase (k_{obs}) was well fit by:

$$k_{obs} = v_o \frac{V_{\max}[Actin]}{K_{\mathrm{ATPase}}+[Actin]} \qquad \textbf{(Equation 1)}$$

From the fit, the actin concentration at half-maximum of the ATPase rate (K_{ATPase}) was determined to be 5.1 ± 0.88 μM, and the maximum ATPase rate (V_{max}) was found to be 3.3 ± 0.15 s^{-1} (Fig, 2B; Table 1).

ATP Binding and ADP Release are Non-Rate Limiting for Myo5 ATPase Activity

The motility rate of many myosins is limited by the rate of actin detachment, and two biochemical transitions, ADP release and subsequent ATP binding, limit the detachment rate. Therefore, we used stopped-flow kinetics to measure ADP release (Fig. 2C, k_{+5}') from and ATP binding to (Fig. 2C, K_1' and k_{+2}') actoMyo5.

We found that yeast Myo5 does not quench the fluorescence of actin labeled at cys-374 with pyrene iodoacetamide, which is the probe most used to measure actomyosin attachment and detachment (De La Cruz and Ostap, 2009). Thus, we measured actoMyo5 detachment by monitoring a decrease in light scattering.

To determine the rate constant for ATP binding, we mixed nucleotide-free actoMyo5 (100 nM) with varying concentrations of ATP and monitored 90° light scattering in the stopped flow instrument. Time courses of light scattering signal followed single exponential decay functions (Fig 2D). For phosphorylated Myo5, the observed rates determined from the exponential fits increased linearly with ATP concentration (Fig. 2E). At concentrations of > 1 mM ATP, the actomyosin complex dissociated within the response time of the instrument, precluding measurement. For unphosphorylated Myo5, the observed rates fit a rectangular hyperbola with increasing ATP concentration (Fig. 2E).

148 The mechanism was modeled as (De La Cruz and Ostap, 2009):

149 $$AM + ATP \overset{K_1'}{\rightleftharpoons} AM(ATP) \overset{k_2'}{\longrightarrow} AM.ATP \overset{k_{diss}}{\longrightarrow} A + M.ATP, \quad \textbf{(Scheme 1)}$$

150

151 where K_1' is a rapid equilibrium binding step, k_2' is a rate-limiting isomerization to the

152 AM.ATP state, and k_{diss} is the rapid actin dissociation step. The apparent second order rate

153 constant for ATP binding to phosphorylated actoMyo5 was determined by a linear fit to the

154 data ($K_1'k_2'$ = 0.39 ± 0.017 μm^{-1} s^{-1}). The unphosphorylated actoMyo5 data were fitted by:

155 $$k_{obs} = \left[\frac{K_1'\,[ATP]}{1 + K_1'\,[ATP]}\right] k_2', \quad \textbf{(Equation 2)}$$

156 and the maximum rate of dissociation (k_2' = 290 ± 24 s^{-1}) and ATP affinities, (K_1' = 0.006 ±

157 0.0016 μM^{-1}) were determined. The apparent second-order rate constant for ATP binding

158 was determined from a linear fit of the observed rates below 100 μM ATP to be $K_1'k_2'$ = 1.1 ±

159 0.28 μM^{-1} s^{-1} (Table 1).

160 The rate constant for ADP dissociation (k_{+5}') was measured by preincubating 100

161 μM ADP with 200 nM actoMyo5 and then rapidly mixing with 2.5 mM ATP as shown in

162 **scheme 2**:

163 $$A.M.ADP \overset{k_5'}{\rightleftharpoons} A.M + ATP \rightleftharpoons A.M(ATP) \longrightarrow A + M.ATP, \quad \textbf{(Scheme 2)}$$

164

165 When myosin active sites are saturated with ADP, the rate of ATP-induced dissociation of

166 actomyosin is limited by the slow dissociation of ADP. Light scattering transients were

167 fitted by single exponential functions, yielding rates for ADP release for phosphorylated

168 actoMyo5 (k_{+5}' = 74 ± 2.0s^{-1}) and for unphosphorylated actoMyo5 (k_{+5}' = 107 ± 5.9 s^{-1}) (Fig.

169 2F and Table 1). The signal-to-noise ratio of the fast light scattering transients is low,

170 resulting in large uncertainties on these fits. However, these rates are substantially faster

than the steady-state ATPase values, but slower than the maximum rate of ATP-induced actomyosin dissociation. ADP release for actoMyo5 ADP is much faster than ADP release for either vertebrate Myo1b or Myo1c (Greenberg et al., 2012; Lewis et al., 2006). It is more similar to the vertebrate Myo5 homologue, Myo1e, which also functions in clathrin-mediated endocytosis (Mezgueldi et al., 2002; Krendel et al., 2007; Cheng et al., 2012). Because ADP release is rate limiting for detachment of Myo5 and Myo1e from actin, these fast values for ADP release mean that the actin-attachment lifetimes for endocytic type I myosins are < 15 ms. This property may make these motors particularly well-suited to function in dynamic actin networks like those at CME sites, where actin filaments elongate and "treadmill" into the cytoplasm (Kaksonen et al., 2003; Picco et al., 2015).

Actin gliding is dependent on Myo5 phosphorylation state

Our kinetic results suggest that both phosphorylated and unphosphorylated Myo5 have low duty ratios (i.e., the motor spends most of its ATPase cycle unbound from actin). Since ADP release limits the rate of phosphorylated Myo5 detachment from actin at saturating ATP (k_{+5}' = 74 ± 2.0 s^{-1}) and since we have measured the overall ATPase rate (V_{max} = 3.3 ± 0.15 s^{-1}), we can estimate the duty ratio:

$$Duty\ Ratio = \frac{\left(\frac{1}{k\prime_5}\right)}{\left(\frac{1}{Vmax}\right)} \qquad \textbf{(Equation 3)}$$

The calculated duty ratios of phosphorylated Myo5 is 0.045, with unphosphorylated Myo5 having a lower duty ratio (< 0.004).

To assess the effect of phosphorylation on Myo5 motility, we performed *in vitro* motility assays at 1 mM ATP. Motors were attached site-specifically to coverslips coated

193 with anti-His_6 antibody. Coverslips were incubated with a range of concentrations of
194 phosphorylated and unphosphorylated Myo5, creating a titration series of surface
195 densities. At low Myo5 surface densities (incubation with ≤ 30 nM phosphorylated Myo5,
196 ≤ 150 nM unphosphorylated Myo5), actin filaments failed to bind the coverslip (Fig. 2G and
197 movies S1 and S2). At higher concentrations, phosphorylated Myo5 moved actin filaments
198 at velocities ranging from 720 ± 40 nm/s (100 nM phosphorylated Myo5) to 880 ± 90 nm/s
199 (40 nM) (Fig. 2G and movie S1). These gliding velocities are considerably higher than those
200 reported by Sun et al., 2006. This may reflect differences in the phosphorylation state of the
201 purified Myo5 protein (see below) or differences in other motility assay conditions, such as
202 light chain availability, which we controlled by including excess Cmd1. Higher (> 5-fold)
203 surface densities of unphosphorylated Myo5 were required to achieve smooth motility, but
204 this motility occurred at a substantially slower speed, ~120 nm/s (Fig. 2G and movie S2).
205 Sun et al., 2006 similarly reported that Myo5 harboring TEDS site mutations moved actin
206 filaments much more slowly. The slower actin gliding speed for unphosphorylated myosin
207 was unexpected given the similar rates of ADP release between phosphorylated and
208 unphosphorylated Myo5 (Table 1). It remains possible that the our kinetics experiments
209 have not determined the rate limiting step for detachment, or more likely that motility of
210 the unphosphorylated myosin is limited by the slow attachment rate of the motor (Stewart
211 et al., 2021), as suggested by the slow actin-activated ATPase rate. The activation of Myo5
212 motility by phosphorylation could explain why fast, cargo-induced endocytosis, which
213 involves rapid and dynamic actin turnover, requires phosphorylated Myo5, while slower
214 constitutive endocytosis does not (Grosshans et al., 2006).
215

Myo5's working stroke comprises two substeps that are consistent with unloaded kinetic measurements

The kinetics of actin attachment durations and mechanics of single myosin molecules were measured using an optical trapping instrument that can detect sub-nanometer displacements with millisecond temporal resolution (Woody et al., 2018; Snoberger et al., 2021). We used the three-bead optical trapping geometry in which a biotinylated actin filament is tethered between two laser-trapped polystyrene beads coated with neutravidin, creating a bead-actin-bead dumbbell (Fig. 3A). Dumbbells were lowered onto pedestal beads that were sparsely coated with phosphorylated Myo5-His_9 bound to a surface-adsorbed anti-His_6 tag antibody. The positions of trapped beads were detected via quadrant photodiode detectors, and single actomyosin binding events were detected by the decrease in covariance of the positions of the two dumbbell beads (Fig. 3B-D).

Traces acquired in the presence of 1, 10, and 1000 μM ATP reveal clear displacements and drops in covariance during actomyosin binding events. Individual points from covariance traces were fit by double gaussian distributions, with the thresholds for event detection indicated as dotted gray lines in Fig. 3 B-D. Event durations clearly decreased with increasing ATP concentrations (Fig. 3 B-D, blue lines).

The myosin-1 working stroke has been shown to occur in two discrete substeps, with the first substep occurring with actin-activated phosphate release, and the second occurring with ADP release (Jontes et al., 1995; Veigel et al., 1999). The substeps can be characterized in optical trapping assays by ensemble averaging single interactions (Veigel et al., 1999; Chen et al., 2012; Laakso et al., 2008), where the detected events are aligned at

238 their beginnings and forward-averaged in time (Fig 3F-H, left), or aligned at their ends and
239 reverse-averaged in time (Fig 3F-H, right).

240 Ensemble averages of Myo5 interactions showed a two-step working stroke at the
241 three ATP concentrations, but the step-size was most accurately resolved at 10 μM ATP
242 (see Materials and Methods). In this condition, an initial substep of 4.8 nm was followed by
243 a second substep of 0.2 nm (Fig. 3G). We determined the lifetimes of the substeps by fitting
244 the ensemble averages with single exponential functions. At 1 μM ATP (Fig. 3F, left trace),
245 the measured rate (> 30 s^{-1}) of the time-forward average was limited by the covariance
246 smoothing window, but at 10 and 1000 μM ATP (Fig. 3 G-H, left traces), the rates were 49 ±
247 1.6 and 50 ± 0.2 s^{-1}, respectively (Fig. 3K) which are similar to the measured ADP release
248 rate (k_{+5}', 74 ± 2.0 s^{-1}, Table 1) supporting the model that the transition from state-1 to
249 state-2 accompanies ADP release.

250 The kinetics of time-reversed averages reveal the lifetime of State 2 (Fig. 3F-H, right
251 traces). Fitting single exponential functions to these traces reveals rates of 0.59 ± 0.003 and
252 7.34 ± 0.1 s^{-1} at 1 and 10 μM ATP, respectively (Fig. 3K). At 1000 μM ATP, the observed rate
253 (> 187 s^{-1}) was limited by the size of the covariance smoothing window (5.25 ms; Fig. 3K).
254 The observed rates at 1 and 10 μM ATP are consistent with the second order rate constant
255 for ATP binding of 0.39 ± 0.0017 $\mu M^{-1}s^{-1}$ measured by stopped-flow kinetics (K_1'k_{+2}',
256 Table 1).

257 We determined the detachment rates of actomyosin events by plotting the
258 cumulative frequency of individual attachment durations and fit a single exponential
259 function to the data by maximum likelihood estimation (Fig. 3I). Data from 1 and 10 μM
260 ATP fit well by single exponentials with rates of 0.88 and 6.87 s^{-1}, respectively (Fig. 3I, Fig.

3K). These rates match well with the observed rate of ATP binding (Table 1), as well as the fits for the reverse ensemble averages, indicating that at sub-saturating ATP (1 and 10 μM), detachment is limited by ATP binding (Figure 3J, blue squares & gray diamonds, Fig. 3K). Data from 1000 μM ATP were best described as the sum of 2 exponentials, with the major rate of 67.8 s^{-1} comprising 92.1% of the total, and a minor rate of 11.6 s^{-1} comprising 7.9% of the total (Fig. 3I, Fig. 3K). The major rate is consistent with both the observed ADP release rate and the measured forward ensemble average rates, indicating that at saturating ATP, ADP release limits detachment of actomyosin interactions (Fig. 3J, blue square and black diamond, Fig. 3K).

Myo5 is a relatively force-insensitive motor

To elucidate the force sensitivity of Myo5, we measured how its actin detachment rate was affected by mechanical force opposing the power stroke using an isometric feedback system that maintained the actin filament near its initial position (Takagi et al., 2006). Because the initial force applied to the myosin during the interaction in this system depends in part on the position on the actin filament that Myo5 binds, which is subject to stochasticity, this approach allowed measurement of Myo5 attachment durations at a range of resistive forces during a single experiment (Fig. 4A). Plotting the attachment durations as a function of force revealed a general trend of longer attachment durations at higher resisting forces. At each given interaction force, the attachment durations are exponentially distributed and, as expected based on prior isometric feedback experiments, the data appear noisy when plotted in this manner (Fig. 4A). Converting these data to

283 detachment rates by binning them by force at every ten points, averaging, and taking the
284 inverse of the attachment duration more clearly reveals the trend (Fig. 4B).
285 To compare the force sensitivity of Myo5 directly to that of other myosins, the force
286 dependence of the Myo5 detachment rate was fit by the Bell Equation:

287 $$k(F) = k_0 \cdot e^{\frac{-F \cdot d}{k_B \cdot T}} \qquad \textbf{(Equation 4)}$$

288 where *k(F)* is the detachment rate at force *F*, k_0 is the detachment rate in the absence of
289 load, *d* is the distance parameter (the distance to the force-dependent transition state and a
290 measure of force sensitivity), k_B is Boltzmann's constant, and *T* is the temperature. Best fit
291 parameters for k_0 and *d* were determined by maximum likelihood estimation of the
292 unaveraged data from Fig. 4A and incorporating the response time (15-30 ms, Woody et al.,
293 2016) yielding an estimated detachment rate in the absence of force of 67.6 s^{-1}, in close
294 agreement with the measured detachment rate under low load conditions at 1000 μM
295 (saturating) ATP (Fig. 3K). The best fit value for the distance parameter, *d*, was 1.14 nm.
296 This distance parameter indicates that Myo5 is much less force sensitive than other
297 characterized type I myosins; the distance parameter for acutely force sensitive rat Myo1b
298 has been measured to be as high as 18 nm for certain splice isoforms (Laakso et al., 2010),
299 and even the moderately force sensitive enzyme Myo1c has a distance parameter of 5.2 nm
300 (Greenberg et al., 2012). Myo5's force sensitivity is more in line with those measured for
301 muscle myosins, like smooth muscle myosin (d = 1.3 nm, Veigel et al., 2003) or β-cardiac
302 myosin (d = 0.97, Greenberg et al., 2014), leading us to characterize Myo5 as a power
303 generating motor, rather than a force sensitive anchor.
304

Proposed function of type I myosin in clathrin-mediated endocytosis

Myo5 has long been known to play a role in clathrin-mediated endocytosis, but the precise mechanistic contribution of the motor has remained obscure (Goodson et al., 1996; Geli and Riezman, 1996). The discovery that both Myo5 and its paralog Myo3 also regulate actin assembly by binding nucleation promoting factors on their non-motor tail only complicated matters (Evangelista et al., 2000; Geli et al., 2000; Lechler et al., 2000). Separating the contributions of the type I myosin motor domain activity from the actin assembly functions of the non-motor tails of these molecules has been stymied by a limited understanding of the motor domain itself.

The data we present here indicate that Myo5's motor domain generates power rather than forming force-sensitive catch bonds. Although the overall ATPase rate of Myo5 is slow relative to other power-generating myosins, its power stroke and detachment from actin are fast, and resistive force slows its power stroke modestly. While Myo5 can complete its working stroke and consume ATP to move actin filaments even when challenged with > 1 pN resistive force, vertebrate Myo1b, a tension-sensitive anchor myosin, stays attached to actin for 50-100 s at 1 pN of load and does not move the filament or consume ATP. Myo5's relative force insensitivity allows it to generate steady power against a wide range of resisting forces/loads. Because Myo3 and Myo5 can each support CME in the absence of the other (Manenschijn et al., 2019), we suspect that Myo3 is a similarly force-insensitive motor. Given the structural and functional homology between Myo5 and vertebrate Myo1e, together with the close agreement of their unloaded kinetics (Mezgueldi et al., 2002), we also predict the Myo1e may also generate biologically relevant power.

328 Myo5's force insensitive kinetics make it most likely that this motor moves actin
329 filaments relative to the membrane at CME sites, which would serve to assist both in
330 plasma membrane invagination and in movement of occluded actin filament barbed ends
331 away from the plasma membrane, creating space for new monomers to assemble
332 (Manenschijn et al., 2019, Fig. 1, right). Myo5 is found mostly near the base of endocytic
333 sites, where the invaginating membrane meets the plasma membrane (Mund et al., 2018;
334 Idrissi et al., 2008). A population of Myo5 has also been localized near the tips of deeply
335 invaginated endocytic pits in immunogold EM studies, but this population of Myo5 is
336 thought to appear only just before scission, after the major work to create the membrane
337 invagination against membrane tension has occurred (Idrissi and Geli, 2014; Idrissi et al.,
338 2008). A related myosin, Myo1c, when membrane-bound, can generate and sustain sub-
339 piconewton forces parallel to the plane of the phospholipid bilayer to which it is bound,
340 and can generate even greater forces when moving actin filaments away from the
341 membrane or when its diffusion within the bilayer is impeded, for example, by other
342 associated proteins (Pyrpassopoulos et al., 2016). Myo5 localized at the base of endocytic
343 invaginations should therefore be capable of binding and moving actin filaments along the
344 invagination axis, which would serve to further invaginate the membrane (Fig. 1, right).
345 Type I myosins are involved in a wide variety of membrane reshaping events in
346 cells, where they often interact with dynamic branched actin networks (Sokac et al., 2006;
347 Almeida et al., 2011; Joensuu et al., 2014; Krendel et al., 2007; Cheng et al., 2012), but the
348 relative contributions of myosin motor activity and actin assembly in these processes have
349 rarely been resolved. Here, we demonstrated that a type I myosin that functions during
350 clathrin-mediated endocytosis, a process well-known to be driven by actin assembly, is also

351 capable of generating power. It might have been the case that this myosin showed force-
352 sensitive binding to actin filaments rather than power generation, which would have
353 implicated this protein as a recruiter and organizer of force-bearing actin filaments at
354 endocytic sites. Our biochemical and biophysical analyses suggest that instead,
355 recruitment of force-bearing actin filaments must be mediated by other actin-binding
356 components of the endocytic actin network, such as the actin-binding protein Sla2 in yeast
357 or Hip1R in mammals, each of which contain a talin-like actin binding domain that may
358 bind actin filaments in a force-sensitive manner (Owen et al., 2022). Implication of
359 endocytic type I myosin as a force-generating protein suggests that actin assembly and
360 myosin power generation can be coordinated to do coherent work in membrane
361 remodeling processes.

Materials and methods

Reagents, proteins, and buffers

ATP concentrations were determined spectrophotometrically after each experiment by absorbance at 259 nm, $\epsilon_{259} = 15{,}400\ M^{-1}cm^{-1}$. Rabbit skeletal muscle actin was prepared and gel filtered (Spudich and Watt, 1971). Actin concentrations were determined spectrophotometrically by absorbance at 290 nm, $\epsilon_{290} = 26{,}600\ M^{-1}cm^{-1}$. All actin was stabilized with one molar equivalent of phalloidin (Sigma). Steady state, transient, and single molecule experiments were performed at 20°C in KMg25 buffer (60 mM MOPS pH 7, 25 mM KCl, 1 mM EGTA, 1 mM $MgCl_2$, 1 mM DTT). Apyrase VII was obtained from Sigma. Purity and concentration of purified proteins were determined by comparing in-gel Coomassie blue staining to staining of known amounts of bovine serum albumin (Pierce).

Expression and Purification of Cmd1

The *S. cerevisiae* calmodulin gene *CMD1* was cloned from genomic DNA into a bacterial expression plasmid with a sequence encoding His_6-TEV situated at the 5' end to generate pDD2743. pDD2743 was transformed into Rosetta *E. coli*, optimized for expression (Novagen). A saturated overnight culture in LB was used to inoculate a 1L culture to OD_{600} = 0.1. Cells were grown to OD_{600} = 0.6-1, induced with 0.5 mM IPTG for 5 hours at 37°C, pelleted at 5,000 rpm for 20 minutes at 4°C, washed with cold 20 mM HEPES pH 7.5, and repelleted at 3,500 rpm for 10 minutes at 4°C in a Jouan CR3i centrifuge. Cell pellets were flash frozen in 45 mL lysis buffer (20 mM HEPES pH 7.5, 1 M KCl, 20 mM Imidazole). Upon thawing, cells were lysed by sonication, 2 mg DNase I (Roche) and triton X-100 to 1% were

385 added, and the resulting lysate was incubated on ice for 30 minutes, then spun at 30,000
386 rpm for 25 minutes in a 70 TI rotor. The supernatant was loaded onto a 1 mL HisTrap HP
387 column (GE healthcare) preequilibrated with binding buffer (20 mM HEPES pH 7.5, 500
388 mM KCl, 20 mM imidazole). The column was washed with 20 mL binding buffer and Cmd1
389 was eluted over a 30 mL 0-100% gradient of elution buffer (20 mM HEPES pH 7.5, 500 mM
390 KCl, 500 mM imidazole). Fractions containing Cmd1 were pooled, Cmd1 was cleaved from
391 His_6 with TEV protease and dialyzed overnight at 4°C into low salt buffer (10 mM Tris pH 7,
392 25 mM NaCl, 2 mM $MgCl_2$, 5 mM DTT). Following dialysis, purified, cleaved Cmd1 was
393 bound to a MonoQ column and eluted over a 10 mL 0-70% gradient of high salt buffer (10
394 mM Tris pH 7, 1 M NaCl, 2 mM $MgCl_2$, 5 mM DTT). Fractions containing Cmd1 were pooled,
395 dialyzed into KMg50 buffer (60 mM MOPS pH 7, 50 mM KCl, 1 mM $MgCl_2$, 1 mM EGTA, 1
396 mM DTT, 5% glycerol), and stored at -80°C.
397

398 **Expression and Purification of Myo5**

399 Myo5 was coexpressed with the myosin chaperone She4 in *S. cerevisiae.* The *MYO5* open
400 reading frame (ORF) from *S. cerevisiae* was cloned from genomic DNA and truncated at
401 Gly^{763}, generating a construct containing the motor domain and both Cmd1-binding IQ
402 motifs of the lever arm. The *SHE4* ORF was cloned in its entirety from *S. cerevisiae* genomic
403 DNA. Both ORFs were ligated into a 2μ expression plasmid with a partially defective *LEU2*
404 gene (*leu2d*) to ensure high copy number, creating plasmid pDD2744 (Roy et al., 2011). The
405 *MYO5* ORF was situated with a sequence encoding AviTag-TEV-His_9 at the 3' end.
406 Expression of the *MYO5* and *SHE4* ORFs was driven by a bidirectional Gal 1/10 promotor.

407 pDD2744 was transformed into D1074 yeast (Roy et al., 2011). Saturated overnight
408 cultures in synthetic minimal medium (1.5 g/L Difacto yeast nitrogen base, 5 g/L
409 ammonium sulfate) supplemented with 2% glucose and dropout uracil and leucine were
410 used to inoculate 1.5 L cultures in the same media with raffinose substituted for glucose to
411 OD_{600} = 0.1. After 18 hours of growth at 30°C, cultures were induced with 2% galactose,
412 Bacto yeast extract was added to 10 g/L, and Bacto peptone to 20 g/L. After 8 hours of
413 expression, the cells were harvested at 5,000 rpm for 10 minutes at 4°C in a TLA3000
414 rotor, washed with 25 mL cold Milli-Q water, repelleted at 3,500 rpm for 10 minutes at 4°C
415 in a Jouan CR3i centrifuge, resuspended in 0.2 volumes of cold Milli-Q water, and drop
416 frozen into liquid nitrogen. Lysis was achieved through cryomilling (10 cycles of 3 minutes
417 grinding with one minute cooldown) in the large vials of a 6870 freezer/mill (SPEX Sample
418 Prep).

419 Cell powders were thawed in binding buffer (10 mM Tris pH 7, 500 mM NaCl, 4 mM
420 $MgCl_2$, 2 mM ATP, 20 mM imidazole, 5 mM DTT) supplemented with 1 mM PMSF, 1 x
421 cOmplete protease inhibitor cocktail without EDTA (Roche), and 1 μM Cmd1. For
422 purification of phosphorylated Myo5, 1 μg Pak1 (Sigma) was included in the lysis buffer
423 and 10 mM β-glycerophosphate, 5 mM sodium pyrophosphate, and 50 mM sodium fluoride
424 were included in all purification buffers. For purification of unphosphorylated Myo5, 4000
425 units lambda phosphatase (NEB) and 1 mM $MnCl_2$ were included in the lysis buffer. The
426 lysate was then spun at 80,000 rpm for 10 minutes at 4°C in a TLA100.3 rotor, filtered
427 through a 0.22 μm filter, and loaded onto a 1 mL HisTrap HP column. The column was
428 washed with wash buffer (Binding buffer with only 200 mM NaCl), and eluted over a 20 mL
429 0-100% gradient of elution buffer (wash buffer with 1 M imidazole).

Fractions containing Myo5 were pooled and supplemented with Cmd1 to 1 μM. For unphosphorylated Myo5 purification, a further 20,000 units lambda phosphatase were added along with $MnCl_2$ to 1 mM and the fractions were incubated at 30°C for 30 minutes. Purified protein was dialyzed through a 3.5 KDa MWCO membrane into 1 L storage buffer (KMg50 with 50% glycerol) overnight at 4°C and again into 500 mL of the same buffer for 2 hours at 4°C, then stored at -20°C.

Kinetic measurements

Kinetic experiments were conducted using an Applied Photophysics (Surrey, UK) SX.18 MV stopped-flow apparatus. To monitor light scattering at 90˚, 450 nm excitation light was used with a 400 nm emission filter. Experimental transients were fit by single exponentials using the software provided with the stopped flow apparatus. 1-7 traces were averaged together to generate each data point. Steady state actin-activated ATPase activity was measured using the NADH enzyme-linked assay (De La Cruz and Ostap, 2009). NADH loss was monitored by absorbance at 340 nm (ϵ_{340} = 6,220 $M^{-1}cm^{-1}$). ATP-induced dissociation of actoMyo5 was measured and analyzed as described (De La Cruz and Ostap, 2009). 0.04 units/mL apyrase was added to solutions of actoMyo5 before mixing to remove contaminating ADP and ATP. Unphosphorylated actoMyo5 required prolonged treatment with apyrase to achieve sufficient signal, presumably because a larger fraction of the population was bound to ATP left over from purification and because the actin-activated ATPase rate of unphosphorylated Myo5 is slow. Concentrations reported are post mixing.

Motility assays

Motility assays were performed essentially as described (Lin et al., 2005). Myo5 was adhered to nitrocellulose coated coverslips via 20 µg anti His_6 antibody (Sigma) blocked with 2 mg/mL casein. Blocking coverslips with bovine serum albumin (BSA) led to inferior gliding. Motility was recorded in the presence of 1 mM Mg^{2+}ATP and 5 µM Cmd1. The rate of actin filament gliding was determined using the manual tracking plugin in Fiji.

Optical trapping

Flow chambers for optical trapping were constructed with double-sided tape and vacuum grease as previously described (Snoberger et al., 2021; Greenberg et al., 2017). Briefly, the coverslip was coated with a 0.1% mixture of nitrocellulose and 2.47 µm diameter silica beads. Coverslips were dried at least 30 minutes and were used within 24 hours of preparation. To define the walls of the flow cell, 2 strips of double-sided tape were placed ~5 mm apart, a 1 mm thick glass slide was placed on top, and carefully sealed with vacuum grease after addition of final buffer.

Trapping buffer (KMg25 with 1 mM DTT freshly added) was used for all trapping assays. A 100x stock of glucose oxidase + catalase (GOC) was freshly prepared by centrifuging catalase (Sigma, > 30000 $U \cdot mL^{-1}$) at 15,000 x g for 1 minute, and adding 2 µl of catalase supernatant to 20 µL of 19.1 $U \cdot \mu L^{-1}$ glucose oxidase (Sigma).

0.01 $mg \cdot mL^{-1}$ anti-His_6 antibody (Sigma) was flowed in the chamber and incubated between 30 seconds and 3 minutes, then immediately blocked with two, 3-minute incubations of 1 - 2 $mg \cdot mL^{-1}$ bovine serum albumin (BSA). Stocks of phosphorylated His_9-tagged Myo5 were diluted to 1 nm in trapping buffer with 300 mM added KCl and

475 incubated in the flow cell for 2 minutes. The number of myosins bound to the surface was
476 limited by the surface concentration of anti-His_6 antibody, and the incubation time of anti-
477 His_6 antibody was adjusted daily between 30 seconds and 3 minutes such that 1 of 3 - 5
478 pedestals tested showed clear myosin interactions with the actin dumbbell.

479 Following incubation with Myo5, a second blocking step with two, 3-minute
480 incubations of 1 - 2 mg/mL BSA was performed. Final buffer added to the flow cell
481 contained trapping buffer with indicated amount of ATP, 1 μL of GOC added immediately
482 prior to addition to chamber, and 0.1 - 0.25 nM rabbit skeletal muscle actin polymerized
483 with 15% biotinylated actin (Cytoskeleton) stabilized by rhodamine-phalloidin (Sigma) at a
484 1.1-1.2 molar ratio with G-actin concentration. Neutravidin-coated beads were prepared by
485 incubating 0.4 ng of 0.8 μm diameter polystyrene beads (Polysciences) and coated with 5
486 mg/mL neutravidin (Thermo Fisher). 3 μL of neutravidin-coated beads were added to one
487 side of the chamber prior to sealing. All trapping data were acquired within 90 minutes of
488 addition of the final buffer to the chamber.

489 Optical trapping experiments assays were performed at room temperature (20 ± 1
490 °C) using a dual beam 1064 nm trapping laser as described in (Woody et al., 2018, 2017). A
491 single laser beam was split into 2 beams using polarizing beam splitters and steered into a
492 60x water immersion objective (Nikon). Laser light was projected through an oil
493 immersion condenser and into quadrant photodiodes (JQ-50P, Electro Optical Components,
494 Inc.), each of which were conjugate to the back focal plane of the objective. Direct force
495 detection from the quadrant photodiodes was achieved using a custom-built high-voltage
496 reverse bias and an amplifier. Data acquisition, beam position control output, and isometric

497 feedback calculations were controlled with custom-built virtual instruments (Labview,
498 Matlab).

499 Individual 0.8 μm diameter neutravidin-coated bead were caught in the two traps
500 and held approximately 5 μm apart. Trap stiffnesses were adjusted to 0.05 – 0.1 pN/nm
501 per trap. A biotinylated actin filament visualized by rhodamine phalloidin was bound to the
502 two trapped beads, creating a bead-actin-bead dumbbell. The dumbbell was pretensioned
503 (3-5 pN) by steering one beam using a piezo controlled mirror conjugate to the back focal
504 plane of the objective, and the surface of pedestal beads were probed for myosins. Putative
505 myosin interactions were detected via drops in variance of the two beads, and the 3-
506 dimensional position of the dumbbell relative to the myosin was refined further by
507 maximizing the rate and size of the observed power stroke deflections. Every 30-60 s, the
508 dumbbell was moved axially along the actin filament in ~6 nm steps between trace
509 acquisition to ensure even accessibility of actin-attachment target zones. Stage drift was
510 corrected via a feedback system using a nano-positioning stage and imaging the position of
511 the pedestal bead with nm precision (Woody et al., 2017). In experiments using 1 μM ATP,
512 due to the longer actomyosin interactions, stage drift was still observed even with the stage
513 feedback engaged, leading to a presumed underestimation of the displacement size. All
514 data were acquired at a sampling rate of 250 kHz.

515 Isometric optical clamping experiments were performed as described in (Woody et
516 al., 2018; Takagi et al., 2006) using a digital feedback loop and a 1-D electro-optical
517 deflector (EOD, LTA4-Crystal, Conoptics) to steer the beam position using input from a high
518 voltage source (Conoptics, Model 420 Amplifier). Briefly, the position of one bead (the
519 "transducer" bead) was maintained at a constant position by adjusting the position of the

other bead (referred to as the “motor” bead) during actomyosin interactions. The response time of the feedback loop during actomyosin interactions was ~15-30 ms.

Optical trap data analysis

Actomyosin interactions for non-isometric optical clamping experiments were detected using the single-molecule computational tool SPASM (Software for Precise Analysis of Single Molecules , Blackwell et al., 2021), which uses a calculation of the dumbbell bead covariances and a change-point algorithm. Data collected at 1000 μM ATP were analyzed at 250 kHz, while data collected at 1 and 10 μM ATP were downsampled to 2 kHz by averaging every 125 points to enhance analysis speed. Events were detected by calculating the covariance of the 2 beads using a smoothing window of 33.3, 15, and 5.25 ms and an averaging window 60, 36, and 12 ms at 1, 10, and 1000 μM ATP, respectively. The instrument deadtime was calculated to be 2 times the covariance averaging window. For each 15 s trace, the detected covariance was plotted and fit to double gaussian distributions, with the smaller mean gaussian corresponding to the actomyosin “bound” portion and the larger mean gaussian corresponding to the “unbound” portion of events. A putative event was defined as an event where the covariance starts above the unbound peak mean, drops below the bound peak mean, and remains below the unbound peak mean for at least the length of the instrument deadtime prior to returning back above unbound peak mean. Event starts and ends were further refined using a changepoint algorithm as described (Blackwell et al., 2021). Attachment durations and ensemble averages of single events were determined using built-in features in the SPASM software. Exponential fits for

542 forward and reverse ensemble averages were performed in Origin 2019 graphing &
543 analysis software (OriginLab).
544 Events detected in isometric optical clamping experiments were detected as
545 described in (Takagi et al., 2006) using a zero crossing analysis via custom MATLAB scripts.
546 Briefly, when a myosin is actively engaged with the dumbbell, force is applied to the
547 transducer bead, a feedback loop is engaged and opposing force applied to the motor bead
548 until the position of the transducer bead is restored. Beginnings of events are defined at
549 the point at which the feedback signal increases from baseline in the motor bead, and ends
550 of events are defined when the feedback signal decreases back below the baseline in the
551 motor bead.

Acknowledgements

We acknowledge Michael Greenberg, Eric Lewellyn, and Akemi Kunibe, each of whom played important roles at the inception of this study. We thank Yale E. Goldman for optical trap instrumentation. We thank Max Ferrin for helpful comments on the manuscript. This work was funded by National Institute of General Medical Sciences (NIGMS) grant R35 GM118149 to D.G.D and grant 5R37GM057247 to E.M.O. R.T.A.P. is currently funded by NIGMS F32 GM142145.

References

Aghamohammadzadeh, S., and K.R. Ayscough. 2009. Differential requirements for actin during yeast and mammalian endocytosis. *Nat. Cell Biol.* 11:1039–1042. doi:10.1038/ncb1918.

Akamatsu, M., R. Vasan, D. Serwas, M. Ferrin, P. Rangamani, and D.G. Drubin. 2020. Principles of self-organization and load adaptation by the actin cytoskeleton during clathrin-mediated endocytosis. *Elife*. 9:1–40. doi:10.7554/eLife.49840.

Almeida, C.G., A. Yamada, D. Tenza, D. Louvard, G. Raposo, and E. Coudrier. 2011. Myosin 1b promotes the formation of post-Golgi carriers by regulating actin assembly and membrane remodelling at the trans-Golgi network. *Nat. Cell Biol.* 13:779–789. doi:10.1038/ncb2262.

Basu, R., E.L. Munteanu, and F. Chang. 2013. Role of turgor pressure in endocytosis in fission yeast. *Mol. Biol. Cell*. 25:679–87. doi:10.1091/mbc.E13-10-0618.

Bement, W.M., and M.S. Mooseker. 1995. TEDS rule: A molecular rationale for differential regulation of myosins by phosphorylation of the heavy chain head. *Cell Motil. Cytoskeleton*. 31:87–92. doi:10.1002/cm.970310202.

Blackwell, T., W.T. Stump, S.R. Clippinger, and M.J. Greenberg. 2021. Computational Tool for Ensemble Averaging of Single-Molecule Data. *Biophys. J.* 120:10–20. doi:10.1016/j.bpj.2020.10.047.

Boulant, S., C. Kural, J.-C. Zeeh, F. Ubelmann, and T. Kirchhausen. 2011. Actin dynamics counteract membrane tension during clathrin-mediated endocytosis. *Nat. Cell Biol.* 13:1124–31. doi:10.1038/ncb2307.

583 Busch, D.J., J.R. Houser, C.C. Hayden, M.B. Sherman, E.M. Lafer, and J.C. Stachowiak. 2015.
584 Intrinsically disordered proteins drive membrane curvature. *Nat. Commun.* 6.
585 doi:10.1038/ncomms8875.
586 Cail, R.C., C.R. Shirazinejad, and D.G. Drubin. 2022. Induced nanoscale membrane curvature
587 bypasses the essential endocytic function of clathrin. *J. Cell Biol.* 221.
588 doi:10.1083/jcb.202109013.
589 Carlsson, A.E. 2018. Membrane bending by actin polymerization. *Curr. Opin. Cell Biol.* 50:1–
590 7. doi:10.1016/j.ceb.2017.11.007.
591 Chen, C., M.J. Greenberg, J.M. Laakso, E.M. Ostap, Y.E. Goldman, and H. Shuman. 2012.
592 Kinetic schemes for post-synchronized single molecule dynamics. *Biophys. J.* 102.
593 doi:10.1016/j.bpj.2012.01.054.
594 Cheng, J., A. Grassart, and D.G. Drubin. 2012. Myosin 1E coordinates actin assembly and
595 cargo trafficking during clathrin-mediated endocytosis. *Mol. Biol. Cell*. 23:2891–904.
596 doi:10.1091/mbc.E11-04-0383.
597 Dannhauser, P.N., and E.J. Ungewickell. 2012. Reconstitution of clathrin-coated bud and
598 vesicle formation with minimal components. *Nat. Cell Biol.* 14:634–639.
599 doi:10.1038/ncb2478.
600 Evangelista, M., B.M. Klebl, A.H. Yong, B.A. Webb, T. Leeuw, E. Leberer, M. Whiteway, D.Y.
601 Thomas, and C. Boone. 2000. A Role for Myosin-I in Actin Assembly through
602 Interactions with Vrp1p, Bee1p, and the Arp2/3 Complex. *J. Cell Biol.* 148:353–362.
603 doi:10.1083/jcb.148.2.353.
604 Geli, M.I., R. Lombardi, B. Schmelzl, and H. Riezman. 2000. An intact SH3 domain is required
605 for myosin I-induced actin polymerization. *EMBO J.* 19:4281–4291.

606 doi:10.1093/emboj/19.16.4281.
607 Geli, M.I., and H. Riezman. 1996. Role of Type I Myosins in Receptor-Mediated Endocytosis
608 in Yeast. *Science*. 272:533–535.
609 Geli, M.I., A. Wesp, and H. Riezman. 1998. Distinct functions of calmodulin are required for
610 the uptake step of receptor-mediated endocytosis in yeast: The type I myosin Myo5p is
611 one of the calmodulin targets. *EMBO J.* 17:635–647. doi:10.1093/emboj/17.3.635.
612 Goodson, H. V, B.L. Anderson, H.M. Warrick, L.A. Pon, and J.A. Spudich. 1996. Synthetic
613 lethality screen identifies a novel yeast myosin I gene (MYO5): myosin I proteins are
614 required for polarization of the actin cytoskeleton. *J. Cell Biol.* 133:1277–1291.
615 doi:10.1083/JCB.133.6.1277.
616 Greenberg, M.J., T. Lin, Y.E. Goldman, H. Shuman, and E.M. Ostap. 2012. Myosin IC generates
617 power over a range of loads via a new tension-sensing mechanism. *Proc. Natl. Acad.*
618 *Sci. U. S. A.* 109:E2433-40. doi:10.1073/pnas.1207811109.
619 Greenberg, M.J., and E.M. Ostap. 2013. Regulation and control of myosin-I by the motor and
620 light chain-binding domains. *Trends Cell Biol.* 23:81–9. doi:10.1016/j.tcb.2012.10.008.
621 Greenberg, M.J., H. Shuman, and E.M. Ostap. 2014. Inherent Force-Dependent Properties of
622 β-Cardiac Myosin Contribute to the Force-Velocity Relationship of Cardiac Muscle.
623 *Biophys. J.* 107:L41–L44. doi:10.1016/j.bpj.2014.11.005.
624 Greenberg, M.J., H. Shuman, and E.M. Ostap. 2017. Measuring the Kinetic and Mechanical
625 Properties of Non-processive Myosins Using Optical Tweezers. *Methods Mol. Biol.*
626 1486:483–509. doi:10.1201/b22505.
627 Grosshans, B.L., H. Grötsch, D. Mukhopadhyay, I.M. Fernández, J. Pfannstiel, F.-Z. Idrissi, J.
628 Lechner, H. Riezman, and M.I. Geli. 2006. TEDS site phosphorylation of the yeast

629 myosins I is required for ligand-induced but not for constitutive endocytosis of the G
630 protein-coupled receptor Ste2p. *J. Biol. Chem.* 281:11104–14.
631 doi:10.1074/jbc.M508933200.
632 Hassinger, J.E., G. Oster, D.G. Drubin, and P. Rangamani. 2017. Design principles for robust
633 vesiculation in clathrin-mediated endocytosis. *Proc. Natl. Acad. Sci. U. S. A.* 114:E1118–
634 E1127. doi:10.1073/pnas.1617705114.
635 Idrissi, F.-Z., and M.I. Geli. 2014. Zooming in on the molecular mechanisms of endocytic
636 budding by time-resolved electron microscopy. *Cell. Mol. Life Sci.* 71:641–57.
637 doi:10.1007/s00018-013-1452-8.
638 Idrissi, F.Z., H. Grötsch, I.M. Fernández-Golbano, C. Presciatto-Baschong, H. Riezman, and
639 M.I. Geli. 2008. Distinct acto/myosin-I structures associate with endocytic profiles at
640 the plasma membrane. *J. Cell Biol.* 180:1219–1232. doi:10.1083/jcb.200708060.
641 Joensuu, M., I. Belevich, O. Rämö, I. Nevzorov, H. Vihinen, M. Puhka, T.M. Witkos, M. Lowe,
642 M.K. Vartiainen, and E. Jokitalo. 2014. ER sheet persistence is coupled to myosin 1c-
643 regulated dynamic actin filament arrays. *Mol. Biol. Cell*. 25:1111–1126.
644 doi:10.1091/mbc.E13-12-0712.
645 Jontes, J.D., E.M. Wilson-Kubalek, and R.A. Milligan. 1995. A 32 degree tail swing in brush
646 border myosin I on ADP release. *Nature*. 378:751–753. doi:10.1038/378751a0.
647 Jusue-Torres, I., R. Tiv, J.C. Ricarte-Filho, A. Mallisetty, L. Contreras-Vargas, M.J. Godoy-
648 Calderon, K. Khaddour, K. Kennedy, K. Valyi-Nagy, O. David, M. Menchaca, A. Kottorou,
649 A. Koutras, F. Dimitrakopoulos, K.M. Abdelhady, M. Massad, I. Rubinstein, L. Feldman, J.
650 Stewart, T. Shimamura, L. Danilova, and A. Hulbert. 2023. Myo1e overexpression in
651 lung adenocarcinoma is associated with increased risk of mortality. *Sci. Rep.* 13:4107.

652 doi:10.1038/s41598-023-30765-y.
653 Kaksonen, M., Y. Sun, and D.G. Drubin. 2003. A pathway for association of receptors,
654 adaptors, and actin during endocytic internalization. *Cell*. 115:475–87.
655 Kaksonen, M., C.P. Toret, and D.G. Drubin. 2005. A modular design for the clathrin- and
656 actin-mediated endocytosis machinery. *Cell*. 123:305–20.
657 doi:10.1016/j.cell.2005.09.024.
658 Kaplan, C., S.J. Kenny, X. Chen, J. Schöneberg, E. Sitarska, A. Diz-Muñoz, M. Akamatsu, K. Xu,
659 and D.G. Drubin. 2022. Load adaptation by endocytic actin networks. *Mol. Biol. Cell*. 33.
660 doi:10.1091/mbc.E21-11-0589.
661 Krendel, M., E.K. Osterweil, and M.S. Mooseker. 2007. Myosin 1E interacts with
662 synaptojanin-1 and dynamin and is involved in endocytosis. *FEBS Lett.* 581:644–50.
663 doi:10.1016/j.febslet.2007.01.021.
664 De La Cruz, E.M., and E.M. Ostap. 2009. Kinetic and Equilibrium Analysis of the Myosin
665 ATPase. *Methods Enzymol.* 455:157–192. doi:10.1016/S0076-6879(08)04206-7.
666 Laakso, J.M., J.H. Lewis, H. Shuman, and E.M. Ostap. 2008. Myosin I can act as a molecular
667 force sensor. *Science*. 321:133–6. doi:10.1126/science.1159419.
668 Laakso, J.M., J.H. Lewis, H. Shuman, and E.M. Ostap. 2010. Control of myosin-I force sensing
669 by alternative splicing. *Proc. Natl. Acad. Sci. U. S. A.* 107:698–702.
670 doi:10.1073/pnas.0911426107.
671 Lechler, T., A. Shevchenko, A. Shevchenko, and R. Li. 2000. Direct involvement of yeast type
672 I myosins in Cdc42-dependent actin polymerization. *J. Cell Biol.* 148:363–373.
673 doi:10.1083/jcb.148.2.363.
674 Lewellyn, E.B., R.T. Pedersen, J. Hong, R. Lu, H.M. Morrison, and D.G. Drubin. 2015. An

675 Engineered Minimal WASP-Myosin Fusion Protein Reveals Essential Functions for
676 Endocytosis. *Dev. Cell*. 35:281–294. doi:10.1016/j.devcel.2015.10.007.
677 Lewis, J.H., T. Lin, D.E. Hokanson, and E.M. Ostap. 2006. Temperature dependence of
678 nucleotide association and kinetic characterization of Myo1b. *Biochemistry*. 45:11589–
679 97. doi:10.1021/bi0611917.
680 Lin, T., N. Tang, and E.M. Ostap. 2005. Biochemical and motile properties of Myo1b splice
681 isoforms. *J. Biol. Chem.* 280:41562–41567. doi:10.1074/jbc.M508653200.
682 Manenschijn, H.E., A. Picco, M. Mund, J. Ries, and M. Kaksonen. 2019. Type-I myosins
683 promote actin polymerization to drive membrane bending in endocytosis. *Elife*.
684 17:490011. doi:10.1101/490011.
685 Mezgueldi, M. El, N. Tang, S.S. Rosenfeld, and E.M. Ostap. 2002. The Kinetic Mechanism of
686 Myo1e (Human Myosin-IC). *J. Biol. Chem.* 277. doi:10.1074/jbc.M200713200.
687 Mogilner, A., and G. Oster. 1996. Cell motility driven by actin polymerization. *Biophys. J.*
688 71:3030–3045. doi:10.1016/S0006-3495(96)79496-1.
689 Mogilner, A., and G. Oster. 2003. Force Generation by Actin Polymerization II: The Elastic
690 Ratchet and Tethered Filaments. *Biophys. J.* 84:1591–1605. doi:10.1016/S0006-
691 3495(03)74969-8.
692 Mund, M., J.A. Van Der Beek, J. Deschamps, S. Dmitrieff, P. Hoess, J.L. Monster, A. Picco, F.
693 Nedelec, M. Kaksonen, and J. Ries. 2018. Systematic Nanoscale Analysis of Endocytosis
694 Links Efficient Vesicle Formation to Patterned Actin Nucleation. *Cell*. 174:884–896.
695 doi:10.1016/j.cell.2018.06.032.
696 Nickaeen, M., J. Berro, T.D. Pollard, and B.M. Slepchenko. 2019. Actin assembly produces
697 sufficient forces for endocytosis in yeast. *Mol. Biol. Cell*. 30:2014–2024.

698 doi:10.1091/mbc.E19-01-0059.

699 Owen, L.M., N.A. Bax, W.I. Weis, and A.R. Dunn. 2022. The C-terminal actin-binding domain
700 of talin forms an asymmetric catch bond with F-actin. *Proc. Natl. Acad. Sci. U. S. A.* 119.
701 doi:10.1073/pnas.2109329119.

702 Pedersen, R.T., and D.G. Drubin. 2019. Type I myosins anchor actin assembly to the plasma
703 membrane during clathrin-mediated endocytosis. *J. Cell Biol.* 218:1138–1147.
704 doi:10.1083/jcb.201810005.

705 Picco, A., M. Mund, J. Ries, F. Nedelec, and M. Kaksonen. 2015. Visualizing the functional
706 architecture of the endocytic machinery. *Elife*. 4:1–29. doi:10.7554/eLife.04535.

707 Pyrpassopoulos, S., G. Arpa?, E.A. Feeser, H. Shuman, E. Tüzel, and E.M. Ostap. 2016. Force
708 generation by membrane-associated myosin-I. *Sci. Rep.* 6:1–14.
709 doi:10.1038/srep25524.

710 Roy, M.A., N. Siddiqui, and D. D'Amours. 2011. Dynamic and selective DNA-binding activity
711 of Smc5, a core component of the Smc5-Smc6 complex. *Cell Cycle*. 10:690–700.
712 doi:10.4161/cc.10.4.14860.

713 Skruzny, M., T. Brach, R. Ciuffa, S. Rybina, M. Wachsmuth, and M. Kaksonen. 2012.
714 Molecular basis for coupling the plasma membrane to the actin cytoskeleton during
715 clathrin-mediated endocytosis. *Proc. Natl. Acad. Sci. U. S. A.* 109:E2533–E2542.
716 doi:10.1073/pnas.1207011109.

717 Snoberger, A., B. Barua, J.L. Atherton, H. Shuman, E. Forgacs, Y.E. Goldman, D.A.
718 Winkelmann, and E.M. Ostap. 2021. Myosin with hypertrophic cardiac mutation r712l
719 has a decreased working stroke which is rescued by omecamtiv mecarbil. *Elife*. 10:1–
720 24. doi:10.7554/eLife.63691.

721 Sokac, A.M., C. Schietroma, C.B. Gundersen, and W.M. Bement. 2006. Myosin-1c couples
722 assembling actin to membranes to drive compensatory endocytosis. *Dev. Cell*. 11:629–
723 40. doi:10.1016/j.devcel.2006.09.002.
724 Spudich, J.A., and S. Watt. 1971. The Regulation of Rabbit Skeletal Muscle Contraction. *J.*
725 *Biol. Chem.* 246:4866–4871.
726 Stewart, T.J., V. Murthy, S.P. Dugan, and J.E. Baker. 2021. Velocity of myosin-based actin
727 sliding depends on attachment and detachment kinetics and reaches a maximum when
728 myosin-binding sites on actin saturate. *J. Biol. Chem.* 297.
729 doi:10.1016/j.jbc.2021.101178.
730 Sun, Y., A.C. Martin, and D.G. Drubin. 2006. Endocytic Internalization in Budding Yeast
731 Requires Coordinated Actin Nucleation and Myosin Motor Activity. *Dev. Cell*. 11:33–46.
732 doi:10.1016/j.devcel.2006.05.008.
733 Takagi, Y., E.E. Homsher, Y.E. Goldman, and H. Shuman. 2006. Force generation in single
734 conventional actomyosin complexes under high dynamic load. *Biophys. J.* 90:1295–
735 1307. doi:10.1529/biophysj.105.068429.
736 Veigel, C., L.M. Coluccio, J.D. Jontes, J.C. Sparrow, R. a Milligan, and J.E. Molloy. 1999. The
737 motor protein myosin-I produces its working stroke in two steps. *Nature*. 398:530–
738 533. doi:10.1038/19104.
739 Veigel, C., J.E. Molloy, S. Schmitz, and J. Kendrick-Jones. 2003. Load-dependent kinetics of
740 force production by smooth muscle myosin measured with optical tweezers. *Nat. Cell*
741 *Biol.* 5:980–986. doi:10.1038/ncb1060.
742 Woody, M.S., M.J. Greenberg, B. Barua, D.A. Winkelmann, Y.E. Goldman, and E.M. Ostap.
743 2018. Positive cardiac inotrope omecamtiv mecarbil activates muscle despite

suppressing the myosin working stroke. *Nat. Commun.* 9. doi:10.1038/s41467-018-06193-2.

Woody, M.S., J.H. Lewis, M.J. Greenberg, Y.E. Goldman, and E.M. Ostap. 2016. MEMLET: An Easy-to-Use Tool for Data Fitting and Model Comparison Using Maximum-Likelihood Estimation. *Biophys. J.* 111:273–282. doi:10.1016/j.bpj.2016.06.019.

Woody, M.S., E.M. Ostap, Y.E. Goldman, and M. Capitanio. 2017. An ultra-fast EOD-based force-clamp detects rapid biomechanical transitions. SPIE-Intl Soc Optical Eng. 26.

Figure 1: Models for the functions of actin assembly and myosin activity during membrane deformation for clathrin-mediated endocytosis

Cartoon diagram illustrating the organization of actin filaments and Myo5 molecules at endocytic sites. Actin filaments are bound by coat proteins at the tip of the growing membrane invagination and oriented with their growing ends toward the plasma membrane, powering membrane invagination. The type I myosin Myo5 could either anchor the actin network in a favorable orientation (left) or provide an assisting force (right).

Figure 2: In-solution, population biochemical characterization of Myo5

(A) Coomassie-stained SDS-polyacrylamide gels showing example preparations of the purified Myo5 motor/lever construct and calmodulin (Cmd1, light chain) used in all experiments. **(B)** The actin concentration dependence of the steady-state ATPase activity of 100 nM unphosphorylated (grey circles) and phosphorylated Myo5 (black circles). Each data point represents the average of 6-7 time courses, which were 100 s each. The orange line is a best fit of the phosphorylated Myo5 data to a rectangular hyperbola. **(C)** Schematic pathway for the Myo5 ATPase cycle. Blue motors are in tightly bound conformations, green motors are weakly bound/unbound. **(D)** Example light scattering transients reporting on ATP-induced dissociation of phosphorylated (left, k_{obs} = 17 s^{-1}) and unphosphorylated (right, k_{obs} = 64.1 s^{-1}) actoMyo5, obtained by mixing 100 nM actoMyo5 (AM) with 94 μm and 72 μM ATP, respectively, as shown in the inset schematic. The black line is the fit of a single exponential function to the data. **(E)** ATP concentration dependence of ATP-induced dissociation of 100 nM unphosphorylated (grey circles) and phosphorylated Myo5 (black circles). Each data point represents 3-6 time courses averaged and fit to a single

exponential decay function. The orange line is a linear best fit of the phosphorylated Myo5 data. The purple line is a best fit of the unphosphorylated Myo5 data to a rectangular hyperbola. **(F)** Example light scattering transients reporting ATP-induced dissociation of ADP-saturated phosphorylated (left) and unphosphorylated (right) actoMyo5, obtained by preincubating 200 nM actoMyo5 (AM) with 100 μM ADP, then mixing rapidly with 2.5 mM ATP, as shown in the inset schematic. The black line the fit of a single exponential function to the data. **(G)** Velocity of actin filament gliding, measured at varying surface densities Phospho-Myo5 (black circles, orange line) and unphosphorylated Myo5 (gray circles, purple line) in *in vitro* motility assays. Myosin concentrations indicate the quantity of protein incubated in the flow chamber before washing. Each data point represents the average velocity of 30 – 60 filaments, and the error bars are standard deviations.

Table 1

Summary of rate and equilibrium constants measured for Myo5 in this study. Errors are standard errors of the fits.

Figure 3: Single molecule, optical trap analysis of Myo5 step size and kinetics

(A) Cartoon schematic of the 3-bead optical trapping setup. A biotinylated actin filament is tethered between two neutravidin-coated beads that are trapped in a dual beam optical trap. This bead-actin-bead "dumbbell" is lowered onto pedestal beads that have been sparsely coated with His_6 antibody to attach Myo5-motor/lever-Avi-Tev-His_9. **(B-D)** Single Myo5 displacements of a single bead and covariance traces, calculated using both beads, showing single molecule interactions acquired in the presence of 1 μM **(B)** 10 μM **(C)** and

798 1000 μM ATP. **(D)**. Blue bars indicate attachment events as identified by covariance (gray)
799 decreases. The threshold of event detection by the covariance traces are indicated by
800 dashed gray lines. **(E)** Schematic of displacement traces depicting the 2-step nature of
801 actomyosin displacements in the optical trap. **(F-H)** Binding events were synchronized at
802 their beginnings (left) or ends (right) and averaged forward or backward in time,
803 respectively. Measured total displacement of Myo5 was 5.0 nm at 10 μM ATP, with the 1st
804 substep contributing a 4.8 nm displacement (arrow 1. in G) and the 2nd substep
805 contributing a 0.2 nm displacement (arrow 2. In G). **(F-H, left)** Forward-averaged
806 ensembles synchronized at the beginnings of events. **(F-H, right)** Reverse-averaged
807 ensembles synchronized at the ends of events. Black and gray lines are single exponential
808 fits in the forward and reverse ensembles, respectively. **(I)** Cumulative distributions of
809 attachment durations for Myo5 at 1, 10, and 1000 μM ATP. Blue lines show cumulative
810 frequency of attachment durations at the indicated ATP concentrations, and the red,
811 yellow, and green lines indicate fitted exponential distributions at 1, 10, and 1000 μM ATP,
812 respectively. 1 and 10 μM ATP were fit well to single exponentials, and the 1000 μM ATP
813 data were best described by the sum of two exponentials. **(J)** Summary of rates at 1, 10, and
814 1000 μM ATP calculated from (F-H). Blue boxes are the fitted exponential distributions
815 from (I), black diamonds are forward ensemble fits from (F-H, left), and gray diamonds are
816 reverse ensemble fits from (F-H, right). At lower concentrations of ATP (1 and 10 μM), the
817 rate of detachment is limited by ATP association, corresponding to the reverse ensemble
818 fits, while at saturating ATP concentration (1000 μM), the detachment rate is limited by the
819 rate of ADP dissociation, corresponding to the forward ensemble fits. **(K)** Summary of rates
820 determined via single molecule optical trapping. Errors for detachment rates are 95%

confidence intervals. Errors for forward and reverse ensemble fits are standard errors of the fits. *Detachment rates at 1000 μM ATP were best fit to the sum of 2 exponents. The major component of the fit (67.8 s^{-1}) comprises 92.1% of the total with the remaining 7.9% having a rate of 11.6 s^{-1}.

Fig 4: Myo5 attachment lifetimes are substantially less force-dependent than other known type I myosins

An isometric optical force clamp was utilized to determine the force-sensitivity of the detachment of Myo5 from actin. **(A)** Durations of individual actomyosin attachments as a function of force, plotted on a semi-log scale **(B)** The solid black line shows the force dependence of the detachment rates determined by MLE fitting of unaveraged points in A. For illustration purposes, attachment durations from (A) were binned by force at every 10 points. Best- fit parameters were determined by MLE fitting and 95% confidence intervals were calculated via bootstrapping. The solid black line is calculated from best fit parameters (k = 67.6 s^{-1}, d = 1.14 nm), while the gray shaded region is the 95% confidence interval (k = 62.4-72.9 s^{-1}, d = 1.03-1.26 nm). All MLE fitting was performed on unaveraged data and was corrected for instrument deadtime.

Movie S1: Motility assays with phosphorylated Myo5

Rhodamine phalloidin-labeled actin filaments gliding over coverslips coated with a concentration series of phosphorylated Myo5 protein in motility buffer with 1 mM ATP. Movies were collected at 1 frame per second and are played back at 16 frames per second.

Movie S2: Motility assays with unphosphorylated Myo5

Rhodamine phalloidin-labeled actin filaments gliding over coverslips coated with a concentration series of unphosphorylated Myo5 protein in motility buffer with 1 mM ATP. Short movies of motility at 100 nM and 150 nM unphosphorylated Myo5 were collected because no motility was observed. Movies at all other concentrations were collected at 1 frame every 4 seconds and are played back at 16 frames per second. The playback rate of Movie S2 is four times faster than the playback rate of Movie S1.

Figure 1

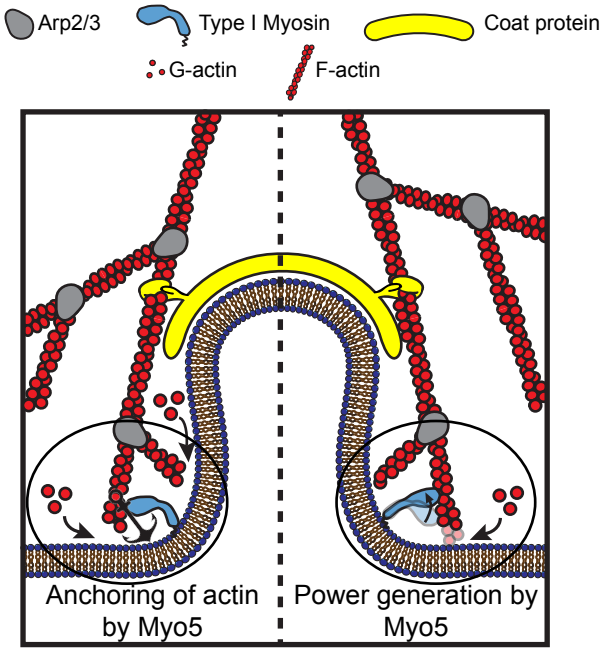
Arp2/3
Type I Myosin
Coat protein
G-actin
F-actin
Anchoring of actin by Myo5
Power generation by Myo5

Figure 2

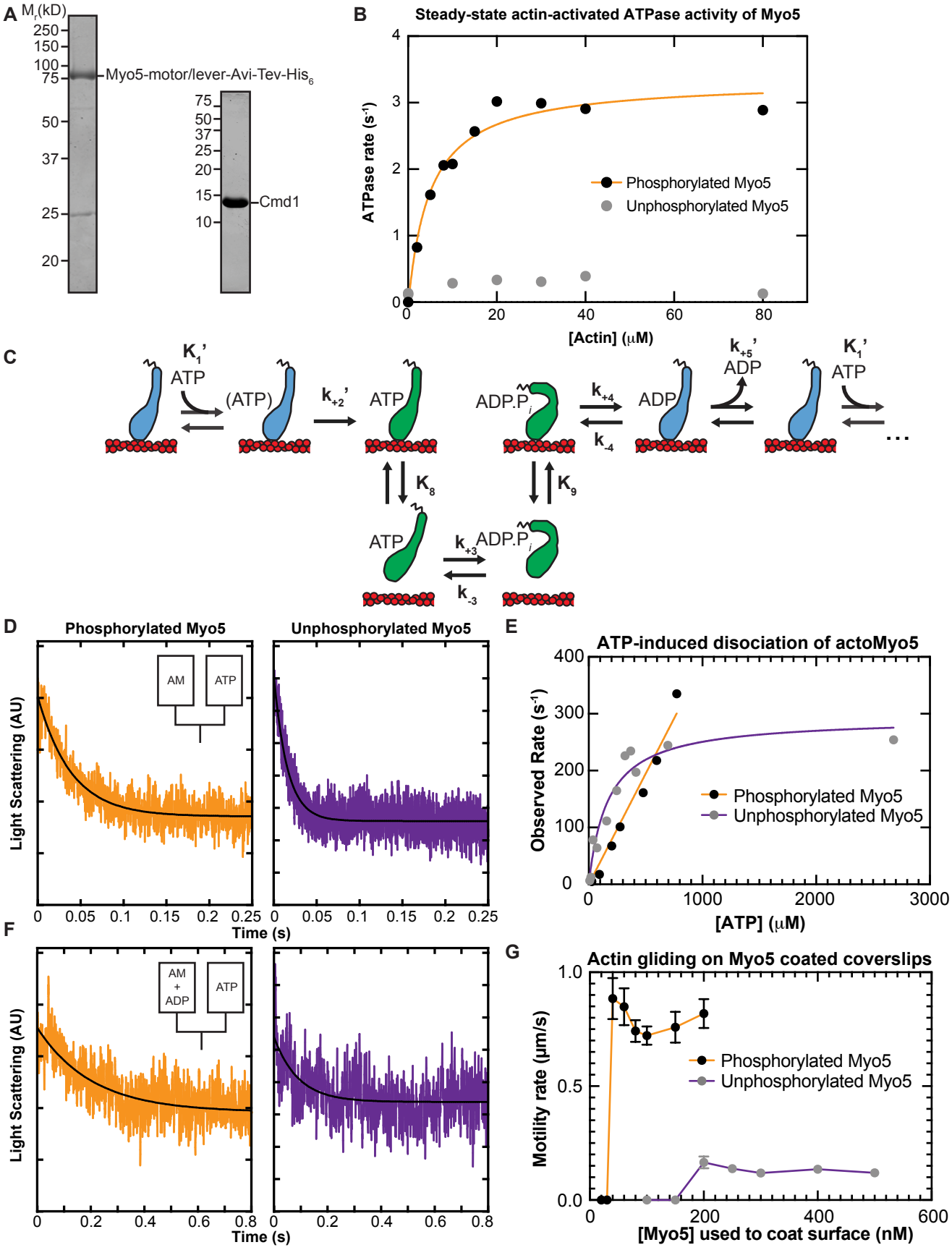
A
Mr(kD)
250
150
100
75
50
37
25
20
Myo5-motor/lever-Avi-Tev-His6
75
50
37
25
20
15
10
Cmd1
B
Steady-state actin-activated ATPase activity of Myo5
ATPase rate (s-1)
[Actin] (μM)
Phosphorylated Myo5
Unphosphorylated Myo5
C
K1'
ATP
(ATP)
k+2'
ATP
ADP.Pi
k+4
k-4
ADP
k+5'
ADP
K1'
ATP
K8
K9
ATP
k+3
ADP.Pi
k-3
D
Phosphorylated Myo5
Unphosphorylated Myo5
AM
ATP
Light Scattering (AU)
Time (s)
E
ATP-induced disociation of actoMyo5
Observed Rate (s-1)
[ATP] (μM)
Phosphorylated Myo5
Unphosphorylated Myo5
F
AM + ADP
ATP
Light Scattering (AU)
Time (s)
G
Actin gliding on Myo5 coated coverslips
Motility rate (μm/s)
[Myo5] used to coat surface (nM)
Phosphorylated Myo5
Unphosphorylated Myo5

Table 1: Rate and equilibrium constants of the Myo5 ATPase cycle

	Phosphorylated Myo5	Unphosphorylated Myo5
Steady-state actin-activated ATPase		
V_{max} (s^{-1})	3.3 (± 0.15)	ND
K_{ATPase} (μM)	5.1 (± 0.88)	ND
ATP binding		
K_1' (μM^{-1})	ND	0.006 (± 0.0016)
k_{+2}' (s^{-1})	≥ 335	290 (± 24)
$K_1'k_{+2}'$ (μM^{-1} s^{-1})[a]	0.39 (± 0.017)[b]	1.1 (± 0.28)[c]
ADP release		
k_{+5}' (s^{-1})	74 (± 2.0)	107 (± 5.9)

[a]Determined from a linear fit of the unbinding rates. [b]Linear fit of all data for Phospho Myo5 in Fig. 2E. [c]Linear fit of observed rates below 100 μM ATP in Fig 2E.

Figure 3

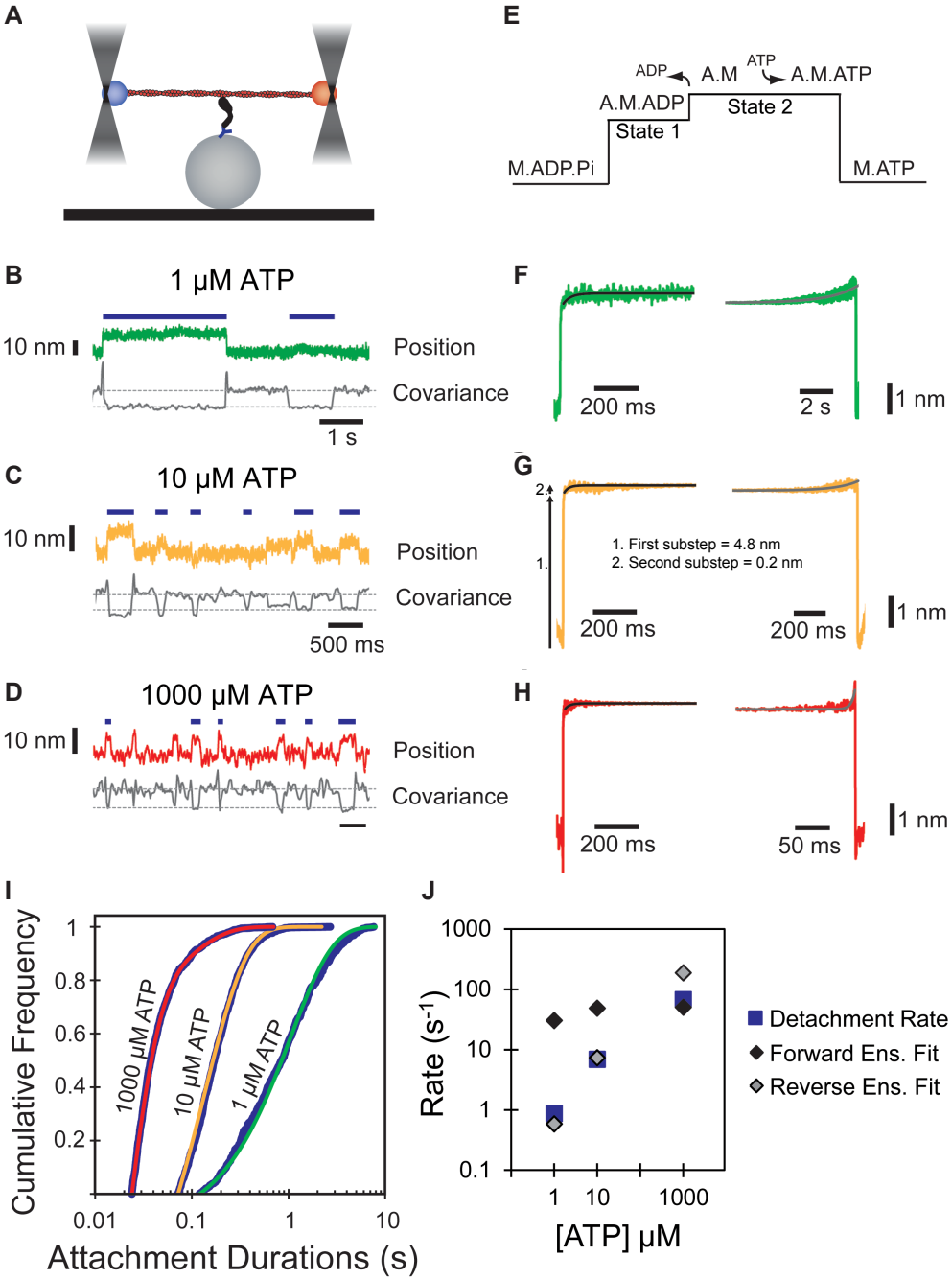

K

Summary of rates determined during single molecule optial trapping

[ATP] μM	Detachment Rate (s^{-1})	Forward Ensemble Fit (s^{-1})	Reverse Ensemble Fit (s^{-1})
1	0.88 (+/- 0.07/0.07)	>30	0.59 (+/- 0.003)
10	6.9 (+/- 0.49/0.46)	49 (+/- 1.6)	7.3 (+/- 0.1)
1000	67.8* (+/- 11.9/8.7)	50 (+/- 0.2)	>187

Figure 4

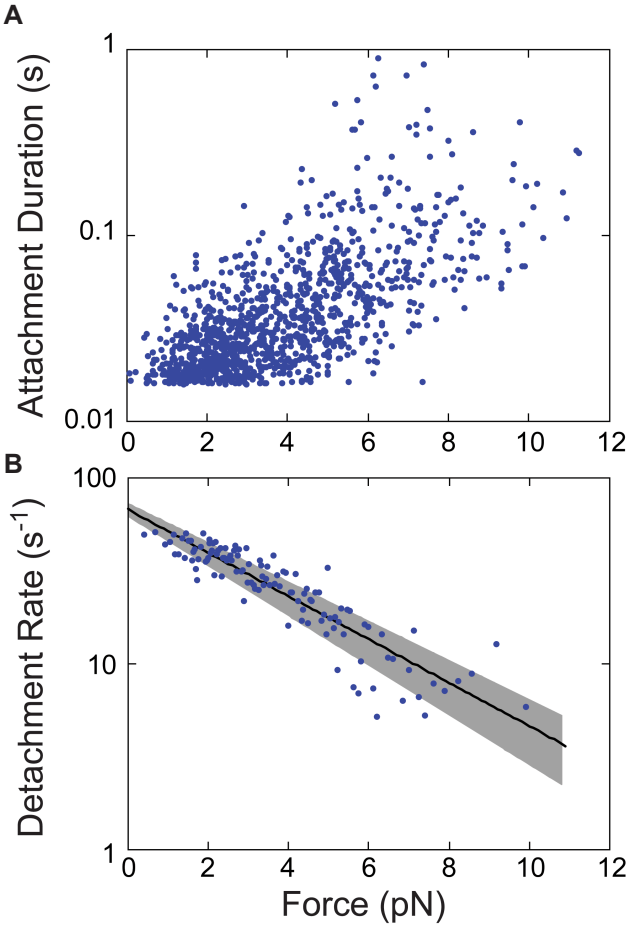
A
Attachment Duration (s)
1
0.1
0.01
0
2
4
6
8
10
12
B
Detachment Rate (s-1)
100
10
1
0
2
4
6
8
10
12
Force (pN)